High-Resolution Quantitative Phase Microscopy with Second-Harmonic Generation and Structured Illumination from a *k*-Space Formulation

Nansen Zhou,[1,†] Andreas Zheng,[1,†] Kenneth K. Y. Wong,[2,3] and Renjie Zhou[1,*]

[1] *Department of Biomedical Engineering, The Chinese University of Hong Kong, Shatin, New Territories, Hong Kong, China*

[2] *Department of Electrical and Electronic Engineering, The University of Hong Kong, Pokfulam Road, Hong Kong, China*

[3] *Advanced Biomedical Instrumentation Centre, Hong Kong Science Park, Shatin, New Territories, Hong Kong, China*

(Received 21 April 2022; revised 25 August 2022; accepted 27 September 2022; published 10 November 2022)

We propose a high-resolution label-free two-dimensional imaging method by introducing second-harmonic generation (SHG) and structured illumination in quantitative phase microscopy (QPM), termed S^2QPM, which can achieve a fourfold lateral resolution improvement compared with normal incident illumination for noncentrosymmetric structures. Unlike traditional QPM only obtaining information about the optical path difference, S^2QPM can additionally recover structural information from the $\chi^{(2)}$ distribution. Analytical solutions for SHG fields are obtained by solving the inhomogeneous and nonlinear Helmholtz equation in the *k*-space in a both concise and accurate way. With the *k*-space SHG field solutions for different structured illumination patterns, an object reconstruction model is developed to retrieve the high-resolution normalized $\chi^{(2)}$ distributions and quantitative phase maps. We simulate high-resolution reconstructions of the normalized $\chi^{(2)}$ distributions and quantitative phase maps using various resolution targets. The lateral resolution improvement is quantified by synthesizing the object spectrum function and profiling resolution targets.

DOI: 10.1103/PhysRevApplied.18.054028

I. INTRODUCTION

In recent years quantitative phase microscopy (QPM) has become an important label-free imaging technique [1,2]. In QPM, the phase shift related to the optical path difference (OPD) at each point across a specimen is mapped through interferometry [3,4] or noninterferometry-based phase-retrieval approaches [5,6]. QPM is suitable for imaging transparent biological samples and profiling fabricated materials structures [3,4]. Over the past decade, many efforts have been made to improve the performance of QPM, including increasing the spatial resolution [7–9], enhancing the phase sensitivity [10,11], and adding molecular specificity through computation and machine learning [12,13]. Very recently, QPM has been applied to many important biomedical studies, such as observation of cell organelles [14,15], characterization of cancer cells [16–18], and classification of leukocyte types [19,20]. However, to further apply QPM for imaging of subcellular structures and their dynamics in cells, the lateral resolution is hindered by the diffraction limit to λ/NA under normal illumination, where NA is the numerical aperture of the system.

To increase the lateral resolution in QPM, illumination angle scanning [9,21] and structured illumination [7,22] have been proposed and demonstrated. However, the spatial resolution is at most improved by a factor of two to $\lambda/2\mathrm{NA}$. Although fluorescence-based imaging techniques can circumvent this limitation to allow structures that are smaller than 100 nm in size to be resolved [23–25], additional sample preparation is required; furthermore, potential photobleaching and phototoxicity during the observation restrict their application scopes [8,12,13]. Therefore, it is critical to explore new strategies to improve the lateral resolution in QPM to retain its label-free advantage. Second-harmonic generation microscopy (SHGM) is a nonlinear and coherent imaging technique in which the wavelength of the incident wave is halved during the second-harmonic generation (SHG) conversion process [8,26]. Using SHGM, label-free imaging of nonlinear biological specimens [27–29] or material samples [30–32] has been demonstrated through mapping their $\chi^{(2)}$ distribution [33]. It has been proposed that a fourfold or higher improvement in resolution can be achieved by combining structured illumination and second-order or higher-order

*rjzhou@cuhk.edu.hk

†These authors contributed equally.

nonlinear processes [34]. However, the physical process of SHG field generation from nonlinear structures was largely unexplored.

To fully understand the imaging process exploring SHG, light-matter interactions in the nonlinear regime need to be modeled and exact solutions of the scattered and unscattered SHG fields are required. The scattered fields can be solved following the conventional integral formulations in three-dimensional (3D) space [35]. Recently, the *k*-space formulation approach has been developed to efficiently solve the wave equations and precisely reveal light-matter interactions in coherent imaging systems, such as optical diffraction tomography [36,37], low-coherence interferometry [38], optical coherence tomography [39], and SHGM [29]. Performing image reconstruction in the *k*-space also offers many advantages over the spatial domain formulation, as the fields can be naturally treated as plane waves of different spatial frequencies, which can be processed more effectively with Fourier transforms [40]. Image reconstruction in the *k*-space has been utilized in structured illumination microscopy (SIM) [41], confocal microscopy [42], synthetic aperture microscopy [43], etc.

In this article, we propose to apply SHG and structured illumination into QPM, namely S^2QPM, to realize label-free high-resolution imaging. A comprehensive *k*-space formulation is proposed to accurately solve the SHG fields under structured illumination. In the *k*-space formulation, we first separate the total SHG field into scattered and unscattered components and solve them from the inhomogeneous and nonlinear Helmholtz equation. The total SHG fields, corresponding to different structured illumination patterns, are then used to reconstruct the normalized $\chi^{(2)}$ distributions and quantitative phase maps of the specimen in the *k*-space. The synthesized object spectrum reveals a fourfold lateral resolution improvement potential. Applying the image reconstruction model on various resolution targets, we further validate the resolution improvement in the spatial domain.

II. WORKING PRINCIPLE OF S^2QPM

A. Conceptual illustration of S^2QPM

The concept of S^2QPM is illustrated in Fig. 1. A laser beam at frequency ω_0 forms a structured illumination, which is s-polarized over the sample. After excitation, the SHG signal at $2\omega_0$ is generated from the sample regions with nonzero nonlinearity coefficients and then collected by an objective lens. The sample SHG field is measured through an interferometer by adding a reference SHG beam. A short-pass filter removes the beams at the fundamental frequency. The interferograms corresponding to different structured illumination orientations are recorded by a camera. After processing the recorded interferograms, a fourfold resolution improvement is expected to be achieved in S^2QPM system when compared with

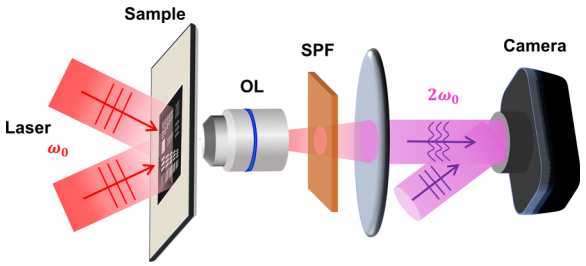

FIG. 1. A conceptual illustration of S^2QPM. OL, objective lens; SPF, short-pass filter.

the linear QPM system with normal illumination. Note that all the structured illumination patterns are maintained at s-polarization, which is possible by inserting a vortex half-wave plate [44]. To generate interferograms at the imaging plane, a linear polarizer is used to ensure the reference beam and the sample beam are the same polarization. Under each structured illumination, only certain elements of the second-order nonlinear susceptibility tensor $\overleftrightarrow{\chi}^{(2)}$ (a total of 27 elements) contribute to the SHG signal [45]. Therefore, the SHG process can be reduced to a scalar wave equation (refer to Appendix A for a full derivation that describes the vectorial SHG process). For nonlinear samples with cylindrical symmetry (e.g., myosin and microtubules [45–47]), an analytical expression for $\chi^{(2)}$ at each point is derived as $\chi^{(2)} = a\cos(\alpha)\cos^2(\psi - \alpha) + b\cos(\alpha) + c\cos(\psi)\cos(\psi - \alpha)$, where a, b, and c are constants, ψ is the polarization angle with respect to the x-axis, and α is the orientation angle of the sample with respect to the x-axis. A full description of the image formation process and the physical model for high resolution object reconstruction in S^2QPM is provided in Secs. II B–II D.

B. Solving SHG fields from the nonlinear Helmholtz equation

Assuming an inhomogeneous medium, the nonlinear Helmholtz equation under the undepleted pump approximation can be written as [26,29]

$$\nabla^2 u(\mathbf{r},\omega) + \omega^2 \frac{n^2(\mathbf{r},\omega)}{c^2} u(\mathbf{r},\omega) = -\frac{\omega^2}{c^2}\chi^{(2)}(\mathbf{r})[u_i(\mathbf{r},\omega) \otimes_\omega u_i(\mathbf{r},\omega)], \quad (1)$$

where $u(\mathbf{r},\omega)$ is the total field which contains the linear field at ω_0 and SHG field at $2\omega_0$, $n(\mathbf{r},\omega)$ is the linear refractive index distribution of an inhomogeneous medium, ω is the angular frequency of light, c is the speed of light in free space, and $\mathbf{r} = (x,y,z) = (\mathbf{r}_\perp, z)$ represents the 3D spatial domain. Assuming the system response is instantaneous, the frequency dependence of $\chi^{(2)}(\mathbf{r})$ can be dropped [26].

The overall SHG process in a thin sample (i.e., thickness much smaller than the photon mean free path to ensure single scattering) can be treated as two subsequent processes, i.e., the incident field first excites the sample to generate the SHG field, namely $u_{\mathrm{SHG}}^{2\omega_0}(\mathbf{r})$, which is then scattered by the sample to generate $u_s^{2\omega_0}(\mathbf{r})$. Here, we only consider the forward propagating fields at $2\omega_0$, and each SHG field component in the k-space can be solved as (details are included in Appendix B)

$$U_{\mathrm{SHG},f}^{2\omega_0}(\mathbf{k}_\perp, z) = \frac{i\beta_2^2}{2\gamma_2} e^{i\gamma_2 z} \otimes_z \{\chi^{(2)}(\mathbf{k}_\perp, z) \otimes_{\mathbf{k}_\perp} \times [U_i(\mathbf{k}_\perp, z) \otimes_{\mathbf{k}_\perp} U_i(\mathbf{k}_\perp, z)]\}, \quad (2a)$$

and

$$U_{s,f}^{2\omega_0}(\mathbf{k}_\perp, z) = \frac{i\beta_2^2}{2\gamma_2} e^{i\gamma_2 z} \otimes_z [\chi(\mathbf{k}_\perp, z) \otimes_{\mathbf{k}_\perp} U_{\mathrm{SHG},f}^{2\omega_0}(\mathbf{k}_\perp, z)], \quad (2b)$$

where $U_{SHG,f}^{2\omega_0}(\mathbf{k}_\perp, z)$ and $U_{s,f}^{2\omega_0}(\mathbf{k}_\perp, z)$ are the 2D Fourier transforms of $u_{\mathrm{SHG}}^{2\omega_0}(\mathbf{r})$ and $u_s^{2\omega_0}(\mathbf{r})$ with respect to $\mathbf{r}_\perp$, $\beta_2 = 2\omega_0/c = 4\pi/\lambda_0$ is the wavenumber of the SHG field in free space, $\gamma_2 = \sqrt{(\overline{n}_2^2\beta_2^2) - |\mathbf{k}_\perp|^2}$ with $\overline{n}_2$ being the spatially averaged refractive index and $\overline{n}_2 = \sqrt{\langle n^2(\mathbf{r}, 2\omega_0)\rangle_r}$, and $\chi(\mathbf{r}) = n^2(\mathbf{r}, 2\omega_0) - \overline{n}_2^2$ is the scattering potential of the object. This result agrees with [29], where tomographic reconstruction of nonlinear structures is demonstrated.

C. Solving the object function from SHG fields under structured illumination

Assuming the incident field is a structured illumination at frequency ω_0, we have

$$U_i(\mathbf{k}_\perp, z) = [\delta(\mathbf{k}_\perp - \mathbf{k}_p)e^{i\phi} + \delta(\mathbf{k}_\perp + \mathbf{k}_p)e^{-i\phi}]e^{i\gamma_p z}, \quad (3)$$

where $\mathbf{k}_p$ is the spatial frequency of the illumination pattern, ϕ is the phase delay that can be adjusted, and $\gamma_p = \sqrt{(\overline{n}_1^2\beta_1^2) - |\mathbf{k}_p|^2}$, with $\beta_1 = \omega_0/c$, and $\overline{n}_1 = \sqrt{\langle n^2(\mathbf{r}, \omega_0)\rangle_r}$ being the spatially averaged refractive index at the fundamental frequency ω_0. For a thin nonlinear structure with a thickness of L (L is assumed to be smaller than the wavelength), we assume the average $\chi^{(2)}(\mathbf{r})$ distribution along the z-axis as $\overline{\chi}^{(2)}(\mathbf{r}_\perp)$. The total SHG field (only measured at one focus plane $z = 0$), summing both the unscattered and scattered components under structured illumination and considering the transfer function of the imaging system, is derived as (details are included in Appendix C)

$$U_{\mathrm{tot}}^{2\omega_0}(\mathbf{k}_\perp, z = 0) = H(\mathbf{k}_\perp) \cdot \{\overline{O}(\mathbf{k}_\perp) \otimes_{\mathbf{k}_\perp} G(\mathbf{k}_\perp)\}, \quad (4)$$

where $G(\mathbf{k}_\perp) = 2\delta(\mathbf{k}_\perp) + \delta(\mathbf{k}_\perp + 2\mathbf{k}_p)e^{-2i\phi} + \delta(\mathbf{k}_\perp - 2\mathbf{k}_p)e^{2i\phi}$, $H(\mathbf{k}_\perp) = \frac{i\beta_2^2 L}{2\gamma_2} A_0(\mathbf{k}_\perp)$ is the transfer function of the imaging system, $A_0(\mathbf{k}_\perp)$ is the circular aperture function of the objective lens, and $\overline{O}(\mathbf{k}_\perp) = \overline{\chi}^{(2)}(\mathbf{k}_\perp) + \frac{i\beta_2^2 L}{2}\overline{\chi}(\mathbf{k}_\perp) \otimes_{\mathbf{k}_\perp} [\frac{1}{\gamma_2}\overline{\chi}^{(2)}(\mathbf{k}_\perp)]$ is the object function that contains the object structural information. Note that to obtain Eq. (4), we assumed a perfect phase matching condition (details in Appendix C). As expressed in Eq. (4), $U_{tot}^{2\omega_0}(\mathbf{k}_\perp)$ contains three shifted object spectrums, i.e., $\overline{O}(\mathbf{k}_\perp)$, $\overline{O}(\mathbf{k}_\perp - 2\mathbf{k}_p)$, $\overline{O}(\mathbf{k}_\perp + 2\mathbf{k}_p)$, each with a radius of $4\pi\mathrm{NA}_{\mathrm{obj}}/\lambda_0 = \beta_2\mathrm{NA}_{\mathrm{obj}}$ ($\mathrm{NA}_{\mathrm{obj}}$ is the numerical aperture of the objective lens) and the shifted frequency amount of $2|\mathbf{k}_p|$, which can reach at most $\beta_2\mathrm{NA}_{\mathrm{obj}}$. To decouple the shifted spectrums, images are captured at three different phase shifts, $\phi = 0$, $\pi/3$, and $2\pi/3$. Applying an inverse Fourier transform over $\overline{O}(\mathbf{k}_\perp)$, we obtain $\overline{O}(\mathbf{r}_\perp)$ as (details are included in Appendix C)

$$\overline{O}(\mathbf{r}_\perp) = \overline{\chi}^{(2)}(\mathbf{r}_\perp) + i\pi\overline{n}_2\beta_2^3 L\overline{\chi}(\mathbf{r}_\perp) \cdot \{\mathrm{sinc}(\overline{n}_2\beta_2\mathbf{r}_\perp) \otimes_{\mathbf{r}_\perp} \overline{\chi}^{(2)}(\mathbf{r}_\perp)\}. \quad (5)$$

Under the assumption of a phase object that exhibits weak absorption, $\overline{\chi}^{(2)}(\mathbf{r}_\perp)$ can be treated as a real function that can be retrieved from the real part of $\overline{O}(\mathbf{r}_\perp)$. Furthermore, when the object has a small refractive index variation relative to the mean at the second-harmonic frequency, namely $n(\mathbf{r}, 2\omega_0) - \overline{n}_2$ is small, we have $\overline{\chi}(\mathbf{r}_\perp) \approx 2\overline{n}_2[n(\mathbf{r}_\perp, 2\omega_0) - \overline{n}_2]$. Then, the phase distribution, defined as $\varphi(\mathbf{r}_\perp) = \beta_2 L[n(\mathbf{r}_\perp, 2\omega_0) - \overline{n}_2]$, can be retrieved from the imaginary part of $\overline{O}(\mathbf{r}_\perp)$ as

$$\overline{O}(\mathbf{r}_\perp) = \overline{\chi}^{(2)}(\mathbf{r}_\perp) + i2\pi(\overline{n}_2\beta_2)^2\varphi(\mathbf{r}_\perp) \cdot \{\mathrm{sinc}(\overline{n}_2\beta_2\mathbf{r}_\perp) \otimes_{\mathbf{r}_\perp} \overline{\chi}^{(2)}(\mathbf{r}_\perp)\}. \quad (6)$$

Further applying paraxial approximation, i.e., $\gamma_2 \approx \overline{n}_2\beta_2$ (with $|\mathbf{k}_\perp| \ll \overline{n}_2\beta_2$), $\overline{O}(\mathbf{r}_\perp)$ can be simplified as

$$\overline{O}(\mathbf{r}_\perp) = \overline{\chi}^{(2)}(\mathbf{r}_\perp)e^{i\varphi(\mathbf{r}_\perp)}. \quad (7)$$

Therefore, $\overline{\chi}^{(2)}(\mathbf{r}_\perp)$ and $\varphi(\mathbf{r}_\perp)$ distribution can be obtained from the amplitude and phase of $\overline{O}(\mathbf{r}_\perp)$, respectively. From this, the spectrums corresponding to different structured illumination patterns can be obtained. After synthesizing the spectrums of $\overline{\chi}^{(2)}(\mathbf{r}_\perp)$ and $\varphi(\mathbf{r}_\perp)$ correspondingly for all illumination patterns, an expanded spectrum with a radius of up to $8\pi\mathrm{NA}_{\mathrm{obj}}/\lambda_0 = 2\beta_2\mathrm{NA}_{\mathrm{obj}}$ is obtained.

D. Testing object reconstruction in a proposed S^{2}QPM system

Based on the SHG field solutions and object reconstruction model, we test the high-resolution object reconstruction process in S^{2}QPM. A proposed experimental design of S^{2}QPM is shown in Fig. 2(a). A laser at $\lambda_0 = 800$ nm is used as the illumination source which is split into the sample beam and the reference beam with a beam splitter, denoted as BS1. In the sample path, a grating, denoted as G, is used to generate multiple diffraction orders, from which the $+1$st and -1st orders are selected in the Fourier plane with a spatial filter (SF) to form the structured illumination at the sample plane. A vortex half-wave plate is inserted after the SF to keep the s-polarization of the patterns with respect to the incident plane [44]. Then the generated SHG signal is collected by an objective lens (OL). In the reference beam, a nonlinear crystal (NLC) is used to generate the SHG signal, whereas a short-pass filter (SPF) is used to filter out the excitation light [29]. With a second beam splitter (BS2) and a polarizer, the sample and reference SHG beams form an interferogram at the final imaging plane, which is captured by a camera. From the interferogram, the complex sample SHG field is retrieved.

Assuming an inhomogeneous object structure, containing groups 10–12 of a USAF target, has a normalized $\overline{\chi}^{(2)}(\mathbf{r}_\perp)$ distribution and an OPD distribution as described in Fig. 2(b.i). OPD is defined as $OPD = [n - n_m]L = \varphi/\beta_2$, where n is the refractive index of the sample and n_m is the average refractive index of the medium at $\lambda_0/2$, and L is the thickness of the sample. Using the proposed experimental system, the interferogram that contains the sample SHG field can be measured. From the spectrum of the interferogram, we select the $+1$st order as illustrated in Fig. 2(b.ii). The $+1$st order contains the complex SHG field under structured illumination as described by Eq. (4). As illustrated in Fig. 2(c.i), in the selected $+1$st-order spectrum, there are also the $+1$st-, 0th-, and -1st-order spectrums due to the structured illumination, which are decoupled using three measurements with phase shifting amount of 0, $\pi/3$, and $2\pi/3$. We repeat this

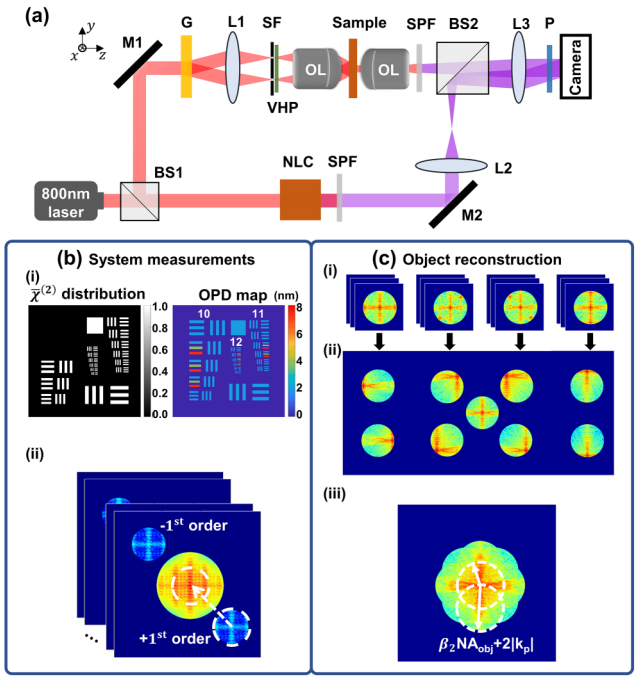

FIG. 2. The object reconstruction process in a proposed S^{2}QPM system. (a) Proposed experimental design of S^{2}QPM. L1-L4, lenses; M1 and M2, mirrors; G, grating; SF, spatial filter; BS, beam splitter; NLC, nonlinear crystal; OL, objective lens; SPF, short-pass filter; VHP, vortex half-wave plate; P, polarizer. (b.i) The $\overline{\chi}^{(2)}(\mathbf{r}_\perp)$ distribution and OPD map of the USAF target used as a sample. (b.ii) The simulated Fourier transform of the interferograms recorded by the camera. The $+1$st order is selected using a filter mask and moved back to the origin for subsequent processing. (c) The individual object spectrums in (c.ii) are retrieved from spectrums of interferograms under different structured illumination patterns shown in (c.i). The spectrums are used to synthesize an expanded spectrum as shown in (c.iii).

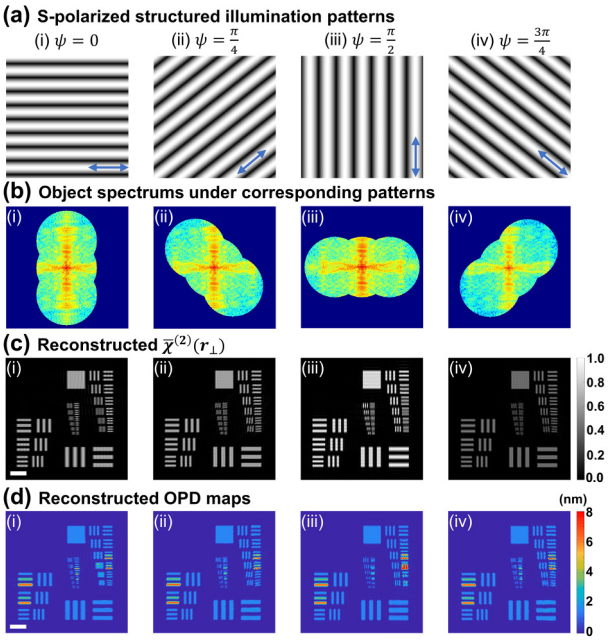

FIG. 3. Illustration of the synthesizing process of the expanded spectrum. Each illumination angle is considered separately first. (a) Structured illumination pattern. The blue arrow indicates the polarization direction. (b) Object spectrums of respective structured illumination patterns. (c) The average $\chi^{(2)}(\mathbf{r})$ distribution along the z-axis $\overline{\chi}^{(2)}(\mathbf{r}_\perp)$ obtained from the real part of Eq. (6). (d) OPD maps obtained as imaginary part of Eq. (6) after filtering them in Fourier space and real space according to $\overline{\chi}^{(2)}(\mathbf{r}_\perp)$. Scale bar: 2 μm.

process for 4 different structured illuminations to obtain the corresponding +1st- and −1st-order object spectrums as illustrated in Fig. 2(c.ii). To explain the imaging process from Fig. 2(c.ii) to Fig.2(c.iii), the processing of each angle while maintaining the s-polarization is shown in Fig. 3. For each structured illumination pattern with corresponding polarization shown in Figs. 3(a.i)–3(a.iv), the synthesized object spectrums along the related directions retrieved according to our scalar model are shown in Figs. 3(b.i)–3(b.iv). These expanded object spectrums are synthesized from the individual object spectrums shown in Fig. 2(c.ii). After taking an inverse Fourier transform for each spectrum, $\overline{O}(\mathbf{r}_\perp)$ corresponding to each pattern is obtained. According to Eq. (6) $\overline{\chi}^{(2)}(\mathbf{r}_\perp)$ can be obtained as the real part of the corresponding $\overline{O}(\mathbf{r}_\perp)$ for each orientation as shown in Figs. 3(c.i)–3(c.iv), whereas the OPD maps in Figs. 3(d.i)–3(d.iv), are obtained from the imaginary part of $\overline{O}(\mathbf{r}_\perp)$ with the knowledge of $\overline{\chi}^{(2)}(\mathbf{r}_\perp)$. Finally, the isotropic resolution improvement of $\overline{\chi}^{(2)}(\mathbf{r}_\perp)$ and OPD map can be achieved by synthesizing the spectrums of the images along different orientations as shown in Fig. 2(c.iii). The spatial resolution improvement on $\overline{\chi}^{(2)}(\mathbf{r}_\perp)$ and OPD maps are verified in Sec. III.

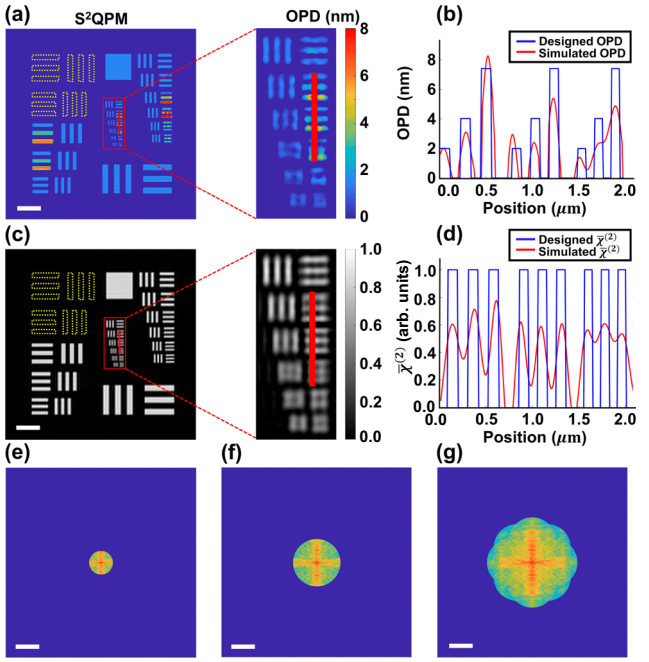

FIG. 4. Simulation of high-resolution imaging on an inhomogeneous USAF target. (a) The retrieved high-resolution OPD map with S^{2}QPM. (b) Line profile of the OPD map along the red line in (a). (c),(d) High-resolution $\overline{\chi}^{(2)}(\mathbf{r}_\perp)$ distribution retrieved with S^{2}QPM and the line profile along the red line. (e)–(g) Spectrums for QPM, SQPM, and S^{2}QPM, respectively. Scale bar: (a),(c) 2 μm, (e)–(g) 2.5 μm^{-1}.

III. SIMULATIONS OF HIGH-RESOLUTION IMAGING

Simulations with $\lambda_0 = 800$ nm and $\mathrm{NA}_{\mathrm{obj}} = 1$ were performed with the above-mentioned inhomogeneous USAF target, a Siemens star object, and a lab logo. The USAF target (group 10–12) as illustrated in Fig. 2(b.i) has structures with line widths between 490 nm and 80 nm. In the simulation, a smaller shifted frequency amount $2|\mathbf{k}_p| = 0.9\beta_2\mathrm{NA}_{\mathrm{obj}}$ is used to mimic a practical experimental situation (i.e., one may not be able to fully utilize the illumination NA). Figures 4(a) and 4(c) show the obtained OPD map and normalized $\overline{\chi}^{(2)}(\mathbf{r}_\perp)$ distribution from S^{2}QPM, respectively, which displays the isotropic resolution enhancement well. The spatial resolution is quantified by analyzing the line profiles along the red line in Figs. 4(a) and 4(c). The line profiles are plotted in Figs. 4(b) and 4(d), from which we estimated that S^{2}QPM achieves a spatial resolution between 200 nm (line width of the 2nd element of group 12 is 100 nm) and 220 nm (line width of the 3rd element of group 12 is 110 nm). The resolution improvement is consistent with our expectation, i.e., a factor of 3.8 improvement. Figures 4(e)–4(g) show the Fourier spectrums of QPM, SQPM, and S^{2}QPM, respectively. When generating the second-harmonic signal, the imaging wavelength is halved, which explains the twofold improvement when comparing QPM and SQPM. In S^{2}QPM, the implementation of structured illumination further enhances the spatial resolution by at most two times.

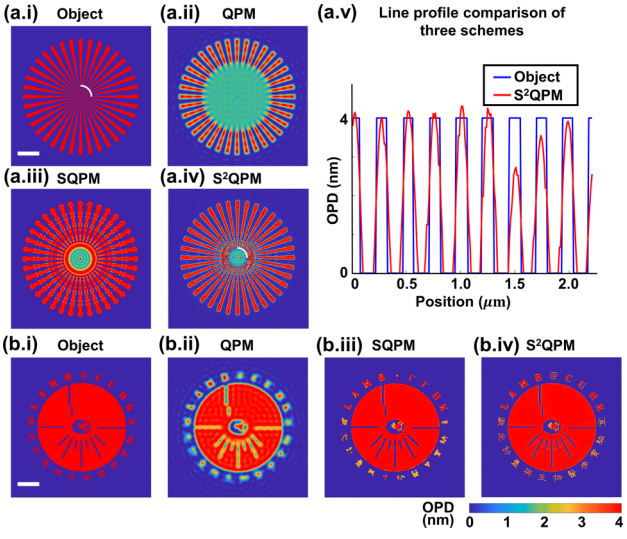

FIG. 5. Simulations of high-resolution imaging on a Siemens star object and a lab logo with homogeneous $\overline{\chi}^{(2)}$ distribution. (a.i) Siemens star object; (a.ii)–(a.iv) OPD maps corresponding to QPM, SQPM, and S^{2}QPM, respectively; (a.v) line profiles along the white circular segment of (a.i) and (a.iv). (b.i) Lab logo (LAMB); (b.ii)–(b.iv) OPD maps corresponding to QPM, SQPM, and S^{2}QPM, respectively. Scale bar in (a.i) and (b.i): 2 μm.

The simulations on a Siemens star object and a lab logo are shown in Fig. 5. Each object is set to have a homogeneous $\overline{\chi}^{(2)}(\mathbf{r}_\perp)$ distribution and a homogeneous OPD map, as illustrated in Figs. 5(a.i) and 5(b.i). When comparing the smallest features resolved in the Siemens star or in the lab logo, the resolution improvement is apparent from QPM under normal illumination [Figs. 5(a.ii) and 5(b.ii)] to SQPM [Figs. 5(a.iii) and 5(b.iii)] and S^2QPM [Figs. 5(a.iv) and 5(b.iv)]. This finding is further quantified by profiling along the white circular segments as indicated in Figs. 5(a.i) and 5(a.iv). From the line profiles in Fig. 5(a.v), it is found that S^2QPM is able to resolve the peaks that are separated by 260 nm, which are otherwise not resolvable under QPM and SQPM. The simulations show a consistent resolution improvement in S^2QPM.

IV. CONCLUSION

We have developed a comprehensive theoretical model for achieving quantitative phase imaging with high resolution on thin specimens. Our model starts from solving the total second-harmonic field from the nonlinear wave equation under structured illumination, which leads to obtaining analytical expressions for $\overline{\chi}^{(2)}(\mathbf{r}_\perp)$ and the phase maps. Our results have also shown that the $\overline{\chi}^{(2)}(\mathbf{r}_\perp)$ and phase map can be obtained from real and imaginary parts of the total field, respectively. Therefore, our proposed S^2QPM method can increase the information capacity of QPM by not only providing fourfold resolution enhancement, but also obtaining sample nonlinearity information from the $\overline{\chi}^{(2)}(\mathbf{r}_\perp)$ distribution. For our simulations, we considered perfect phase matching, which is experimentally valid for uniaxial crystals and interfaces [33,45]. However, under most practical scenarios, phase matching is imperfect so that the efficiency of the SHG conversion will drop. In our case, the SHG intensity will be modulated by a factor of $\mathrm{sinc}[(2\gamma_p - \gamma_2)L/2]$, where $\gamma_p = \sqrt{(\overline{n_1}^2\beta_1^2) - |\mathbf{k_p}|^2}$ and $\gamma_2 = \sqrt{(\overline{n_2}^2\beta_2^2) - |\mathbf{k}_\perp|^2}$ (see Appendix C for details). Under imperfect phase matching, the interpretation of the retrieved phase will be more complex, which is why we limit our model to thin samples. Overall, this proposed new label-free 2D imaging method can be potentially implemented for high-resolution imaging of thin material structures and thin biological specimens by exploring both the linear and nonlinear sample information.

ACKNOWLEDGMENTS

R. Z. acknowledges the financial support from Hong Kong Innovation and Technology Fund (Grant Nos. ITS/148/20 and ITS/178/20FP), Croucher Foundation (CM/CT/CF/CIA/0688/19ay), and Research Grant Council of Hong Kong SAR (Grant No. 14209521). K. K. Y. W. acknowledges the financial support from the Research Grants Council of the Hong Kong Special Administrative Region of China (HKU 17210522, HKU C7074-21G, HKU 17205321, HKU 17200219, HKU 17209018, CityU T42-103/16-N) and Health@InnoHK program of the Innovation and Technology Commission of the Hong Kong SAR Government.

APPENDIX A: VECTORIAL SHG PROCESS

We first define a fixed x-y-z coordinate system, where z is the optical axis of the imaging system. In the SHG process, the second-order nonlinear susceptibility is treated as a third rank tensor $\overleftrightarrow{\chi}^{(2)}$, where 18 out of the 27 elements are independent. The second-order nonlinear polarization field $\mathbf{P}_{\mathrm{NL}}^{(2)}$ can be written as [45]

$$\begin{bmatrix} P_{NL,x}^{(2)} \\ P_{NL,y}^{(2)} \\ P_{NL,z}^{(2)} \end{bmatrix} = \epsilon_0 \begin{bmatrix} \chi_{xxx}^{(2)} & \chi_{xyy}^{(2)} & \chi_{xzz}^{(2)} & \chi_{xyz}^{(2)} & \chi_{xxz}^{(2)} & \chi_{xxy}^{(2)} \\ \chi_{yxx}^{(2)} & \chi_{yyy}^{(2)} & \chi_{yzz}^{(2)} & \chi_{yyz}^{(2)} & \chi_{yxz}^{(2)} & \chi_{yxy}^{(2)} \\ \chi_{zxx}^{(2)} & \chi_{zyy}^{(2)} & \chi_{zzz}^{(2)} & \chi_{zyz}^{(2)} & \chi_{zxz}^{(2)} & \chi_{zxy}^{(2)} \end{bmatrix} \begin{bmatrix} u_x^2 \\ u_y^2 \\ u_z^2 \\ 2u_y u_z \\ 2u_x u_z \\ 2u_x u_y \end{bmatrix}, \tag{A1}$$

where $\chi_{jkl}^{(2)}(j,k,l = x,y,z)$ is the component of the tensor, and u_x, u_y, and u_z are the components of the incident field $\mathbf{u}_i = u_x\mathbf{e}_x + u_y\mathbf{e}_y + u_z\mathbf{e}_z$. As the structured illumination is kept at s-polarization for all different orientations, the polarization axis is always parallel to the orientation of the fringes. For a particular fringe orientation ψ with respect to the x-axis (note that $\psi = 0, \pi/4, \pi/2, 3\pi/4$ for the four different orientations), the incident vector field is $\mathbf{u}_i = u_i[\cos(\psi)\mathbf{e}_x + \sin(\psi)\mathbf{e}_y] = u_x\mathbf{e}_x + u_y\mathbf{e}_y$. Assuming a nonlinear sample with cylindrical symmetry (e.g., myosin and microtubules [46,47]), $\mathbf{P}_{\mathrm{NL}}^{(2)}$ can be simplified to [45]

$$\mathbf{P}_{\mathrm{NL}}^{(2)} = \epsilon_0[a\hat{\boldsymbol{\tau}}(\hat{\boldsymbol{\tau}}\cdot\mathbf{u}_i)^2 + b\hat{\boldsymbol{\tau}}(\mathbf{u}_i\cdot\mathbf{u}_i) + c\mathbf{u}_i(\hat{\boldsymbol{\tau}}\cdot\mathbf{u}_i)], \tag{A2}$$

where $\hat{\boldsymbol{\tau}} = \cos(\alpha)\mathbf{e}_x + \sin(\alpha)\mathbf{e}_y$ is defined along the symmetrical axis of the sample, which has an angle of α with respect to the x-axis, shown in Fig. 6; here a, b, c are coefficients related to the tensor elements in $\overleftrightarrow{\chi}^{(2)}$. A linear polarizer oriented at the x-axis is placed in front of the camera, which will ensure that the x component of $\mathbf{P}_{\mathrm{NL}}^{(2)}$ is obtained. Based on Eq. (A2), $P_{\mathrm{NL},x}^{(2)}(\mathbf{r},t)$ is formulated as

$$\begin{aligned} P_x^{(2)}(\mathbf{r},t) &= \epsilon_0[a\cos(\alpha)\cos^2(\psi-\alpha) + b\cos(\alpha) \\ &\quad + c\cos(\psi)\cos(\psi-\alpha)]u_i^2(\mathbf{r},t) \\ &= \epsilon_0\chi_\psi^{(2)}(\mathbf{r})u_i^2(\mathbf{r},t), \end{aligned} \tag{A3}$$

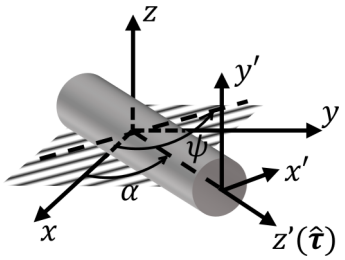

FIG. 6. A nonlinear sample with cylindrical symmetry and orientation in the xy plane with an angle α with respect to the x-axis. A x'-y'-z' coordinate is defined with z' along the symmetry axis.

where $\chi^{(2)}_{\psi}(\mathbf{r})$ is the second-order nonlinear susceptibility recovered in the simulations for each structured illumination pattern with fringe orientation ψ. The above formulations provide a basis to reduce the vectorial nature of the SHG process to a scalar description. Furthermore, Eq. (A3) provides a possibility to obtain the values of a, b, c, and α for every sample point by fitting this equation with measurements at different ψ from 0° to 360°. For more details and discussions on retrieving the second-order nonlinear susceptibility, refer to Ref. [46] and Appendix D.

APPENDIX B: SOLVING THE SHG FIELDS FROM THE NONLINEAR WAVE EQUATION

Considering an inhomogeneous medium, the scalar wave equation can be written as [26]

$$\nabla^2 u(\mathbf{r},t) - \frac{n^2(\mathbf{r})}{c^2}\frac{\partial^2 u(\mathbf{r},t)}{\partial t^2} = \mu_0 \frac{\partial^2 P_{\mathrm{NL}}(\mathbf{r},t)}{\partial t^2}, \tag{B1a}$$

where $u(\mathbf{r},t)$ is the total field, $c = 1/\sqrt{\epsilon_0\mu_0}$ is the speed of light in free space, μ_0 is the magnetic permeability in free space, ϵ_0 is the electric permittivity of free space, and $P_{\mathrm{NL}}(\mathbf{r},t)$ is the nonlinear polarization field. Considering only the second-order polarization field component in accordance with Appendix A, we have

$$P_{\mathrm{NL}}(\mathbf{r},t) = \epsilon_0 \chi^{(2)}(\mathbf{r}) u^2(\mathbf{r},t), \tag{B1b}$$

where $\chi^{(2)}(\mathbf{r})$ is a function related to the second-order nonlinear susceptibility tensor elements and the orientation angle of the sample and illumination patterns, which is a constant in time when assuming an instantaneous response. Note that, the subscript ψ is omitted in the following derivation when considering a particular linear polarization and illumination pattern. Under this assumption, the nonlinear polarization field only depends on the instantaneous value of the electric field [26]. Transforming Eq. (B1a) into the $(\mathbf{r},\omega)$ domain, we have

$$\nabla^2 u(\mathbf{r},\omega) + \frac{\omega^2 n^2(\mathbf{r},\omega)}{c^2} u(\mathbf{r},\omega) = -\mu_0 \omega^2 P_{\mathrm{NL}}(\mathbf{r},\omega), \tag{B2a}$$

$$P_{\mathrm{NL}}(\mathbf{r},\omega) = \epsilon_0 \chi^{(2)}(\mathbf{r})[u(\mathbf{r},\omega) \otimes_\omega u(\mathbf{r},\omega)], \tag{B2b}$$

where $n(\mathbf{r},\omega)$ is the linear refractive index of the inhomogeneous media, ω is the angular frequency of light, and $\otimes_\omega$ denotes the convolution operator with respect to ω. For SHG under the undepleted pump approximation [26], only the incident light at the fundamental frequency, namely $u_i(\mathbf{r},\omega=\omega_0)\delta(\omega-\omega_0)$, contributes to the nonlinear polarization field, thus making $P_{\mathrm{NL}}(\mathbf{r},\omega) = \epsilon_0\chi^{(2)}(\mathbf{r})[u_i^2(\mathbf{r},\omega=\omega_0)\delta(\omega-2\omega_0)]$. The δ function conforms to the normalization principle: $\int_{-\infty}^{+\infty}\delta(\omega)d\omega = 1$. As a result, the total field $u(\mathbf{r},\omega)$, as described in Eq. (B2a), can be separated into the linear field and SHG field components as $u(\mathbf{r},\omega) = u(\mathbf{r},\omega=\omega_0)\delta(\omega-\omega_0) + u(\mathbf{r},\omega=2\omega_0)\delta(\omega-2\omega_0)$. Then, Eq. (B2a) can be rewritten as

$$\begin{aligned}&[\nabla^2 + \frac{\omega^2 n^2(\mathbf{r},\omega)}{c^2}][u(\mathbf{r},\omega=\omega_0)\delta(\omega-\omega_0)\\ &\quad + u(\mathbf{r},\omega=2\omega_0)\delta(\omega-2\omega_0)]\\ &\quad = -\mu_0\epsilon_0\omega^2\chi^{(2)}(\mathbf{r})[u_i^2(\mathbf{r},\omega=\omega_0)\delta(\omega-2\omega_0)].\end{aligned} \tag{B3}$$

Considering only the SHG field ($\omega = 2\omega_0$) components in Eq. (B3) we have

$$\begin{aligned}&[\nabla^2 + \frac{\omega^2 n^2(\mathbf{r},\omega)}{c^2}][u(\mathbf{r},\omega=2\omega_0)\delta(\omega-2\omega_0)]\\ &\quad = -\mu_0\epsilon_0\omega^2\chi^{(2)}(\mathbf{r})[u_i^2(\mathbf{r},\omega=\omega_0)\delta(\omega-2\omega_0)].\end{aligned} \tag{B4}$$

Integrating over ω for both sides of Eq. (B4) results in

$$\begin{aligned}&[\nabla^2 + (\frac{2\omega_0}{c})^2 n^2(\mathbf{r},\omega=2\omega_0)]u^{2\omega_0}(\mathbf{r})\\ &\quad = -\left(\frac{2\omega_0}{c}\right)^2 \chi^{(2)}(\mathbf{r})u_i^2(\mathbf{r}),\end{aligned} \tag{B5}$$

where $u^{2\omega_0}(\mathbf{r})$ denotes the total SHG field at $2\omega_0$. We define $\beta_2 = 2\omega_0/c$ as the wavenumber of the SHG field in free space. Then, Eq. (B5) can be rewritten as

$$\begin{aligned}&\nabla^2 u^{2\omega_0}(\mathbf{r}) + \beta_2^2 n^2(\mathbf{r},\omega=2\omega_0)u^{2\omega_0}(\mathbf{r})\\ &\quad = -\beta_2^2\chi^{(2)}(\mathbf{r})u_i^2(\mathbf{r}).\end{aligned} \tag{B6}$$

Equation (B6) is consistent with the result in [29]. The total SHG field $u^{2\omega_0}(\mathbf{r})$ can be split into the unscattered SHG field and scattered SHG field components, i.e., $u^{2\omega_0}(\mathbf{r}) = u^{2\omega_0}_{SHG}(\mathbf{r}) + u^{2\omega_0}_s(\mathbf{r})$. This is because the light-matter interaction process involving the SHG fields can be treated as two processes, i.e., the incident field first excites the sample and generates the SHG field, namely $u^{2\omega_0}_{SHG}(\mathbf{r})$, which is then scattered by the sample to generate $u^{2\omega_0}_s(\mathbf{r})$, so Eq. (B6) can

be separated into two equations to describe each process as

$$\nabla^2 u_{\mathrm{SHG}}^{2\omega_0}(\mathbf{r}) + \overline{n_2}^2\beta_2^2 u_{\mathrm{SHG}}^{2\omega_0}(\mathbf{r}) = -\beta_2^2\chi^{(2)}(\mathbf{r})u_i{}^2(\mathbf{r}), \quad \text{(B7a)}$$

$$\nabla^2 u_s^{2\omega_0}(\mathbf{r}) + \overline{n_2}^2\beta_2^2 u_s^{2\omega_0}(\mathbf{r}) = -\chi(\mathbf{r})\beta_2^2[u_{SHG}^{2\omega_0}(\mathbf{r}) + u_s^{2\omega_0}(\mathbf{r})], \quad \text{(B7b)}$$

where $\overline{n_2} = \sqrt{\langle n^2(\mathbf{r}, 2\omega_0)\rangle_r}$ is the spatially averaged refractive index and $\chi(\mathbf{r}) = n^2(\mathbf{r}, 2\omega_0) - \overline{n_2}^2$ is the scattering potential of the medium. Assuming the scattered SHG field is much weaker than the unscattered SHG field, i.e., $u_s^{2\omega_0}(\mathbf{r}) \ll u_{\mathrm{SHG}}^{2\omega_0}(\mathbf{r})$, then we have

$$\nabla^2 u_s^{2\omega_0}(\mathbf{r}) + \overline{n_2}^2\beta_2^2 u_s^{2\omega_0}(\mathbf{r}) = -\beta_2^2\chi(\mathbf{r})u_{\mathrm{SHG}}^{2\omega_0}(\mathbf{r}). \quad \text{(B7c)}$$

To solve the SHG fields, we first take the Fourier transforms with respect to $\mathbf{r}$ over Eqs. (B7a) and (B7c) as

$$(\overline{n_2}^2\beta_2^2 - k^2)U_{\mathrm{SHG}}^{2\omega_0}(\mathbf{k}) = -\beta_2^2[\chi^{(2)}(\mathbf{k}) \otimes U_i(\mathbf{k}) \otimes U_i(\mathbf{k})], \quad \text{(B8a)}$$

$$(\overline{n_2}^2\beta_2^2 - k^2)U_s^{2\omega_0}(\mathbf{k}) = -\beta_2^2[\chi(\mathbf{k}) \otimes U_{\mathrm{SHG}}^{2\omega_0}(\mathbf{k})], \quad \text{(B8b)}$$

where $\mathbf{k} = (k_x, k_y, k_z) = (\mathbf{k}_\perp, k_z)$, and $\otimes$ is the convolution operator over the $\mathbf{k}$ domain. Then the SHG fields are solved as

$$\begin{aligned} U_{\mathrm{SHG}}^{2\omega_0}(\mathbf{k}) &= \frac{-\beta_2^2}{(\overline{n_2}^2\beta_2^2 - |\mathbf{k}_\perp|^2 - k_z^2)} \\ &\quad \times [\chi^{(2)}(\mathbf{k}) \otimes U_i(\mathbf{k}) \otimes U_i(\mathbf{k})] \\ &= \frac{\beta_2^2}{2\gamma_2}\left(\frac{1}{k_z - \gamma_2} - \frac{1}{k_z + \gamma_2}\right) \\ &\quad \times [\chi^{(2)}(\mathbf{k}) \otimes U_i(\mathbf{k}) \otimes U_i(\mathbf{k})], \end{aligned} \quad \text{(B9a)}$$

$$\begin{aligned} U_s^{2\omega_0}(\mathbf{k}) &= \frac{-\beta_2^2}{(\overline{n_2}^2\beta_2^2 - |\mathbf{k}_\perp|^2 - k_z^2)}[\chi(\mathbf{k}) \otimes U_{\mathrm{SHG}}^{2\omega_0}(\mathbf{k})] \\ &= \frac{\beta_2^2}{2\gamma_2}\left(\frac{1}{k_z - \gamma_2} - \frac{1}{k_z + \gamma_2}\right)[\chi(\mathbf{k}) \otimes U_{\mathrm{SHG}}^{2\omega_0}(\mathbf{k})], \end{aligned} \quad \text{(B9b)}$$

where $\gamma_2 = \sqrt{(\overline{n_2}^2\beta_2^2) - |\mathbf{k}_\perp|^2}$ and $1/(k_z - \gamma_2)$ and $1/(k_z + \gamma_2)$ represent forward and backward propagation, respectively. In the proposed S^{2}QPM system, we only consider the forward scattering fields, denoted as $u_{\mathrm{SHG},f}^{2\omega_0}$ and $u_{s,f}^{2\omega_0}$, thus only selecting the $1/(k_z - \gamma_2)$ component. Note that $\mathcal{F}^{-1}(1/k_z - \gamma_2) = ie^{i\gamma_2 z}\mathrm{sgn}(z)$, where sgn is the sign function. Next, we take the inverse Fourier transform of the forward components with respect to k_z that results in

$$\begin{aligned} U_{\mathrm{SHG},f}^{2\omega_0}(\mathbf{k}_\perp, z) &= \frac{i\beta_2^2}{2\gamma_2}e^{i\gamma_2 z} \otimes_z \{\chi^{(2)}(\mathbf{k}_\perp, z) \otimes_{\mathbf{k}_\perp} \\ &\quad \times [U_i(\mathbf{k}_\perp, z) \otimes_{\mathbf{k}_\perp} U_i(\mathbf{k}_\perp, z)]\}, \end{aligned} \quad \text{(B10a)}$$

$$\begin{aligned} U_{s,f}^{2\omega_0}(\mathbf{k}_\perp, z) &= \frac{i\beta_2^2}{2\gamma_2}e^{i\gamma_2 z} \otimes_z \\ &\quad \times [\chi(\mathbf{k}_\perp, z) \otimes_{\mathbf{k}_\perp} U_{\mathrm{SHG},f}^{2\omega_0}(\mathbf{k}_\perp, z)], \end{aligned} \quad \text{(B10b)}$$

where $\otimes_z$ represents the convolution over the z-dimension. In the next step, we derive the SHG fields in the context of structured illumination.

APPENDIX C: DERIVING THE TOTAL SHG FIELD UNDER STRUCTURED ILLUMINATION

The structured illumination at the fundamental frequency, as the sum of the +1st and −1st diffraction orders from the grating, can be described as

$$U_i(\mathbf{k}_\perp, z) = [\delta(\mathbf{k}_\perp - \mathbf{k_p})e^{i\phi} + \delta(\mathbf{k}_\perp + \mathbf{k_p})e^{-i\phi}]e^{i\gamma_p z}, \quad \text{(C1)}$$

where $\mathbf{k_p}$ is the spatial frequency of the pattern which is related to the grating period, ϕ is the phase delay that can be adjusted by translating the grating, $\gamma_p = \sqrt{(\overline{n_1}^2\beta_1^2) - |\mathbf{k_p}|^2}$ is the longitudinal wavenumber, $\beta_1 = \omega_0/c$, and $\overline{n_1} = \sqrt{\langle n^2(\mathbf{r}, \omega_0)\rangle_r}$ is the spatially averaged refractive index at the fundamental frequency. Using this expression for $u_i(\mathbf{k}_\perp, z)$ as described in Eq. (C1), the convolution of the input fields in Eq. (B10a) results in

$$\begin{aligned} &U_i(\mathbf{k}_\perp, z) \otimes_{\mathbf{k}_\perp} U_i(\mathbf{k}_\perp, z) \\ &\quad = [\delta(\mathbf{k}_\perp - \mathbf{2k_p})e^{2i\phi} + \delta(\mathbf{k}_\perp + \mathbf{2k_p})e^{-2i\phi} + 2\delta(\mathbf{k}_\perp)]e^{2i\gamma_p z}. \end{aligned} \quad \text{(C2)}$$

To simplify the following formulations, define

$$G(\mathbf{k}_\perp) = G_0(\mathbf{k}_\perp) + G_1(\mathbf{k}_\perp) + G_{-1}(\mathbf{k}_\perp), \quad \text{(C3)}$$

where $G_0(\mathbf{k}_\perp) = 2\delta(\mathbf{k}_\perp)$, $G_1(\mathbf{k}_\perp) = \delta(\mathbf{k}_\perp + \mathbf{2k_p})e^{-2i\phi}$, and $G_{-1}(\mathbf{k}_\perp) = \delta(\mathbf{k}_\perp - \mathbf{2k_p})e^{2i\phi}$. Substituting Eq. (C2) into Eq. (B10a), the SHG field can be written as

$$\begin{aligned} &U_{\mathrm{SHG},f}^{2\omega_0}(\mathbf{k}_\perp, z) \\ &\quad = \frac{i\beta_2^2}{2\gamma_2}e^{i\gamma_2 z} \otimes_z \{e^{2i\gamma_p z}\,[\chi^{(2)}(\mathbf{k}_\perp, z) \otimes_{\mathbf{k}_\perp} G(\mathbf{k}_\perp)]\}. \end{aligned} \quad \text{(C4)}$$

For a thin nonlinear structure with a thickness of L, we assume the $\chi^{(2)}(\mathbf{r})$ distribution after averaging over the z-axis as $\overline{\chi}^{(2)}(\mathbf{r}_\perp)$. Considering only the

$G_0(\mathbf{k}_\perp)$ component in Eq. (C4), the convolution with respect to z can be processed as $e^{i\gamma_2 z}\otimes_z[e^{2i\gamma_p z}\chi^{(2)}(\mathbf{k}_\perp,z)] = e^{i\gamma_2 z}\int_{-L/2}^{L/2}\chi^{(2)}(\mathbf{k}_\perp,z')e^{i(2\gamma_p-\gamma_2)z'}dz' = e^{i\gamma_2 z}\overline{\chi}^{(2)}(\mathbf{k}_\perp)\int_{-\frac{L}{2}}^{\frac{L}{2}}e^{i(2\gamma_p-\gamma_2)z'}dz'$. Note that: $\int_{-\frac{L}{2}}^{\frac{L}{2}}e^{i(2\gamma_p-\gamma_2)z'}dz' = L\mathrm{sinc}[\frac{(2\gamma_p-\gamma_2)L}{2}] \approx L$. Then, Eq. (C4) can be expressed as

$$U^{2\omega_0}_{\mathrm{SHG},f}(\mathbf{k}_\perp,z) = \frac{i\beta_2^2 L}{2\gamma_2}e^{i\gamma_2 z}\overline{\chi}^{(2)}(\mathbf{k}_\perp)\otimes_{\mathbf{k}_\perp}G(\mathbf{k}_\perp). \quad \text{(C5)}$$

Substituting Eq. (C5) into Eq. (B10b) and noting that the convolution along z is evaluated as $e^{i\gamma_2 z}\otimes_z[\chi(\mathbf{k}_\perp,z)e^{i\gamma_2 z}] = e^{i\gamma_2 z}\overline{\chi}(\mathbf{k}_\perp)L$, the forward scattered SHG field is then expressed as

$$U^{2\omega_0}_{s,f}(\mathbf{k}_\perp,z) = \frac{i\beta_2^2 L}{2\gamma_2}e^{i\gamma_2 z}\left\{\frac{i\beta_2^2 L}{2}\overline{\chi}(\mathbf{k}_\perp)\otimes_{\mathbf{k}_\perp} \times\left[\frac{1}{\gamma_2}\overline{\chi}^{(2)}(\mathbf{k}_\perp)\otimes_{\mathbf{k}_\perp}G(\mathbf{k}_\perp)\right]\right\}. \quad \text{(C6)}$$

For an imaging system, the aperture function $A_0(\mathbf{k}_\perp)$ determines the maximum detectable spatial frequency. We assume $A_0(\mathbf{k}_\perp)$ as a circle function with a radius of $2\pi\mathrm{NA}_{\mathrm{obj}}/\lambda_{\mathrm{em}}$, where λ_{em} is the emission wavelength, and for SHG $\lambda_{\mathrm{em}} = \lambda_0/2$. The total SHG field at the imaging plane ($z=0$), is a summation of the SHG field and the scattering field and can be described as

$$U^{2\omega_0}_{\mathrm{tot}}(\mathbf{k}_\perp,z=0) = \frac{i\beta_2^2 L}{2\gamma_2}A_0(\mathbf{k}_\perp)\left[\overline{\chi}^{(2)}(\mathbf{k}_\perp)\otimes_{\mathbf{k}_\perp}G(\mathbf{k}_\perp) + \frac{i\beta_2^2 L}{2} \times\overline{\chi}(\mathbf{k}_\perp)\otimes_{\mathbf{k}_\perp}\left[\frac{1}{\gamma_2}\overline{\chi}^{(2)}(\mathbf{k}_\perp)\otimes_{\mathbf{k}_\perp}G(\mathbf{k}_\perp)\right]\right]. \quad \text{(C7)}$$

To provide the total SHG field with an explicit physical meaning, we rewrite it as

$$U^{2\omega_0}_{\mathrm{tot}}(\mathbf{k}_\perp,z=0) = H(\mathbf{k}_\perp)\cdot\{\overline{O}(\mathbf{k}_\perp)\otimes_{\mathbf{k}_\perp}G(\mathbf{k}_\perp)\}, \quad \text{(C8)}$$

where $H(\mathbf{k}_\perp) = \frac{i\beta_2^2 L}{2\gamma_2}A_0(\mathbf{k}_\perp)$ is the transfer function of the imaging system, and $\overline{O}(\mathbf{k}_\perp) = \overline{\chi}^{(2)}(\mathbf{k}_\perp) + \frac{i\beta_2^2 L}{2}\overline{\chi}(\mathbf{k}_\perp)\otimes_{\mathbf{k}_\perp}[\frac{1}{\gamma_2}\overline{\chi}^{(2)}(\mathbf{k}_\perp)]$ the object function. Equation (C8) contains the object spectrum that is shifted to $\overline{O}(\mathbf{k}_\perp-\mathbf{2k_p})$, $\overline{O}(\mathbf{k}_\perp+\mathbf{2k_p})$, and $\overline{O}(\mathbf{k}_\perp)$, which can be solved with three image acquisitions at three different phase shifts. By shifting the spectrum back to its original position, one can reconstruct the object spectrum function with an expanded cutoff spatial frequency of $4\pi\mathrm{NA}_{\mathrm{obj}}/\lambda_0 + 2|\mathbf{k}_p| = 2\beta_2\mathrm{NA}_{obj}$ along the illumination pattern direction. Next, applying the inverse Fourier transform over $\overline{O}(\mathbf{k}_\perp)$, we have

$$\overline{O}(\mathbf{r}_\perp) = \overline{\chi}^{(2)}(\mathbf{r}_\perp) + \frac{i\beta_2^2 L}{2}\overline{\chi}(\mathbf{r}_\perp)\mathcal{F}^{-1}\left\{\frac{1}{\gamma_2}\overline{\chi}^{(2)}(\mathbf{k}_\perp)\right\}. \quad \text{(C9)}$$

For the inverse Fourier transform of $1/\gamma_2$,

$$\begin{aligned}\mathcal{F}^{-1}\{\frac{1}{\gamma_2}\} &= \frac{1}{\overline{n_2}\beta_2}\iint\frac{1}{\sqrt{1-(\frac{|\mathbf{k}_\perp|}{\overline{n_2}\beta_2})^2}}e^{ik_x x+ik_y y}dk_x dk_y \\ &= \frac{2\pi}{\overline{n_2}\beta_2}\int_0^{\overline{n_2}\beta_2}\frac{1}{\sqrt{1-(\frac{k_\perp}{\overline{n_2}\beta_2})^2}}J_0(k_\perp r_\perp)k_\perp dk_\perp \\ &= 2\pi\overline{n_2}\beta_2\int_0^1\frac{1}{\sqrt{1-q^2}}J_0(\overline{n_2}\beta_2 q r_\perp)qdq \\ &= 2\pi\overline{n_2}\beta_2\mathrm{sinc}(\overline{n_2}\beta_2 r_\perp). \end{aligned} \quad \text{(C10)}$$

Here $|\mathbf{k}_\perp| = k_\perp = \sqrt{k_x^2+k_y^2}$, $|\mathbf{r}_\perp| = r_\perp = \sqrt{x^2+y^2}$, $q = k_\perp/\overline{n_2}\beta_2$. For the inverse Fourier transform of $1/\sqrt{1-(|\mathbf{k}_\perp|/\overline{n_2}\beta_2)^2}$, it is assumed that $|\mathbf{k}_\perp| < \overline{n_2}\beta_2$, which is reasonable, because only the far field is considered. According to the integration: $\int_0^1\frac{qJ_0(qy)}{(1-q^2)^{1/2}}dq = \mathrm{sinc}(y)$ [48]. Then, Eq. (C9) becomes

$$\overline{O}(\mathbf{r}_\perp) = \overline{\chi}^{(2)}(\mathbf{r}_\perp) + i\pi\overline{n_2}\beta_2^3 L\overline{\chi}(\mathbf{r}_\perp)\cdot\{\mathrm{sinc}(\overline{n_2}\beta_2 r_\perp)\otimes_{\mathbf{r}_\perp}\overline{\chi}^{(2)}(\mathbf{r}_\perp)\}. \quad \text{(C11)}$$

Equation (C11) is the most accurate form that describes the object function. Next, we look at the object function under special assumptions that are often used in practical situations.

(i) When the object is transparent, namely a phase object that exhibits nearly no absorption, $\chi^{(2)}(\mathbf{r}_\perp)$ is approximated as a real function. It is also true that the refractive index fluctuations are small relative to the mean at the second harmonic frequency, $n(\mathbf{r},2\omega_0) - \overline{n_2}$ is typically small, so $\overline{\chi}(\mathbf{r}_\perp) \approx 2\overline{n_2}[n(\mathbf{r}_\perp,2\omega_0) - \overline{n_2}]$. Then Eq. (C11) can be rewritten as

$$\overline{O}(\mathbf{r}_\perp) = \overline{\chi}^{(2)}(\mathbf{r}_\perp) + i2\pi(\overline{n_2}\beta_2)^2\varphi(\mathbf{r}_\perp)\cdot\{\mathrm{sinc}(\overline{n_2}\beta_2 r_\perp)\otimes_{\mathbf{r}_\perp}\overline{\chi}^{(2)}(\mathbf{r}_\perp)\}. \quad \text{(C12)}$$

From Eq. (C12), $\overline{\chi}^{(2)}(\mathbf{r}_\perp)$ can be obtained as the real part of $\overline{O}(\mathbf{r}_\perp)$, while the phase term $\varphi(\mathbf{r}_\perp) = \beta_2 L[n(\mathbf{r}_\perp,2\omega_0) - \overline{n_2}]$ can be obtained from the imaginary part of $\overline{O}(\mathbf{r}_\perp)$.

(ii) On the basis of (i), when the imaging system deploys low-NA optics (NA < 0.7 [49]), $|\mathbf{k}_\perp|$ is small that

$\gamma_2 \approx \bar{n}_2\beta_2$. Then, we can further simplify $\overline{O}(\mathbf{r}_\perp)$ as

$$\overline{O}(\mathbf{r}_\perp) = \overline{\chi}^{(2)}(\mathbf{r}_\perp) + i\beta_2^2 L\bar{n}_2[n(\mathbf{r}_\perp, 2\omega_0) - \bar{n}_2]\cdot \mathcal{F}^{-1}\left\{\frac{1}{\bar{n}_2\beta_2}\overline{\chi}^{(2)}(\mathbf{k}_\perp)\right\} = \{\overline{\chi}^{(2)}(\mathbf{r}_\perp)\cdot[1 + i\varphi(\mathbf{r}_\perp)]\!]. \tag{C13}$$

Further, with the assumption of a thin object, $e^{ix} \approx 1 + ix$ when $x \ll 1$ (i.e., $\beta_2 L[n(\mathbf{r}_\perp, 2\omega_0) - \bar{n}_2] \ll 1$), we have

$$\overline{O}(\mathbf{r}_\perp) = \overline{\chi}^{(2)}(\mathbf{r}_\perp)e^{i\varphi(\mathbf{r}_\perp)}. \tag{C14}$$

From Eq. (C14), we can see that $\overline{\chi}^{(2)}(\mathbf{r}_\perp)$ and $\phi(\mathbf{r}_\perp)$ distributions can be obtained from amplitude and phase parts of $\overline{O}(\mathbf{r}_\perp)$, respectively.

APPENDIX D: DISCUSSION

Here we further discuss the meaning of the coefficients a, b and c. When $u_z = 0$, only three elements $\chi^{(2)}_{xxx}, \chi^{(2)}_{xxy}, \chi^{(2)}_{xyy}$ matter in the calculation of $P^{(2)}_{\mathrm{NL},x}(\mathbf{r}, t)$. With the coordinate transformation to account for the sample orientation with respect to the xyz coordinate system [45],

$$\begin{bmatrix}\chi^{(2)}_{y'y'z'}\\ \chi^{(2)}_{z'y'y'}\\ \chi^{(2)}_{z'z'z'}\end{bmatrix} = \begin{bmatrix}2g & g & d\\ f-h & -h & h\\ -2g & d & g\end{bmatrix}^{-1}\begin{bmatrix}\chi^{(2)}_{xxx}\\ \chi^{(2)}_{xxy}\\ \chi^{(2)}_{xyy}\end{bmatrix}, \tag{D1}$$

where $\chi^{(2)}_{y'y'z'}$, $\chi^{(2)}_{z'y'y'}$, and $\chi^{(2)}_{z'z'z'}$ are the tensor elements in the local nonlinear sample coordinate system, $g = \sin^2(\alpha)\cos(\alpha)$, $h = \cos^2(\alpha)\sin(\alpha)$, $d = \cos^3(\alpha)$ and $f = \sin^3(\alpha)$. With this transformation, Eqs. (A1), and (A3), the form of a, b, and c can be expressed based on $\chi^{(2)}_{j'k'l'}$:

$$a = \chi^{(2)}_{z'z'z'} - 2\chi^{(2)}_{y'y'z'} - \chi^{(2)}_{z'y'y'}, \tag{D2a}$$

$$b = \chi^{(2)}_{z'y'y'}, \tag{D2b}$$

$$c = 2\chi^{(2)}_{y'y'z'}. \tag{D2c}$$

These equations show that a, b, and c can be regarded as local constants independent of the polarization of the field.

[1] Y. Park, C. Depeursinge, and G. Popescu, Quantitative phase imaging in biomedicine, Nat. Photonics **12**, 578 (2018).

[2] G. Popescu, *Quantitative Phase Imaging of Cells and Tissues* (McGraw-Hill Education, New York City, 2011).

[3] B. Bhaduri, C. Edwards, H. Pham, R. Zhou, T. H. Nguyen, L. L. Goddard, and G. Popescu, Diffraction phase microscopy: principles and applications in materials and life sciences, Adv. Opt. Photonics **6**, 57 (2014).

[4] X. Chen, M. E. Kandel, and G. Popescu, Spatial light interference microscopy: principle and applications to biomedicine, Adv. Opt. Photonics **13**, 353 (2021).

[5] X. Ou, R. Horstmeyer, C. Yang, and G. Zheng, Quantitative phase imaging via Fourier ptychographic microscopy, Opt. Lett. **38**, 4845 (2013).

[6] D. Paganin and K. A. Nugent, Noninterferometric phase imaging with partially coherent light, Phys. Rev. Lett. **80**, 2586 (1998).

[7] S. Chowdhury and J. Izatt, Structured illumination quantitative phase microscopy for enhanced resolution amplitude and phase imaging, Biomed. Opt. Express **4**, 1795 (2013).

[8] V. Micó, J. Zheng, J. Garcia, Z. Zalevsky, and P. Gao, Resolution enhancement in quantitative phase microscopy, Adv. Opt. Photonics **11**, 135 (2019).

[9] C. Zheng, D. Jin, Y. He, H. Lin, J. Hu, Z. Yaqoob, P. T. C. So, and R. Zhou, High spatial and temporal resolution synthetic aperture phase microscopy, Adv. Photonics **2**, 065002 (2020).

[10] Y. Nie and R. Zhou, Beating temporal phase sensitivity limit in off-axis interferometry based quantitative phase microscopy, APL Photonics **6**, 011302 (2021).

[11] Z. Yaqoob, W. Choi, S. Oh, N. Lue, Y. Park, C. Fang-Yen, R. R. Dasari, K. Badizadegan, and M. S. Feld, Improved phase sensitivity in spectral domain phase microscopy using line-field illumination and self phase-referencing, Opt. Express **17**, 10681 (2009).

[12] Y. N. Nygate, M. Levi, S. K. Mirsky, N. A. Turko, M. Rubin, I. Barnea, G. Dardikman-Yoffe, M. Haifler, A. Shalev, and N. T. Shaked, Holographic virtual staining of individual biological cells, Proc. Natl. Acad. Sci. **117**, 9223 (2020).

[13] M. E. Kandel, Y. R. He, Y. J. Lee, T. H.-Y. Chen, K. M. Sullivan, O. Aydin, M. T. A. Saif, H. Kong, N. Sobh, and G. Popescu, Phase imaging with computational specificity (PICS) for measuring dry mass changes in sub-cellular compartments, Nat. Commun. **11**, 6256 (2020).

[14] S. Guo, Y. Ma, Y. Pan, Z. J. Smith, and K. Chu, Organelle-specific phase contrast microscopy enables gentle monitoring and analysis of mitochondrial network dynamics, Biomed. Opt. Express **12**, 4363 (2021).

[15] D. Dong, X. Huang, L. Li, H. Mao, Y. Mo, G. Zhang, Z. Zhang, J. Shen, W. Liu, Z. Wu, G. Liu, Y. Liu, H. Yang, Q. Gong, K. Shi, and L. Chen, Super-resolution fluorescence-assisted diffraction computational tomography reveals the three-dimensional landscape of the cellular organelle interactome, Light: Sci. Appl. **9**, 11 (2020).

[16] Y. Li, M. J. Fanous, K. A. Kilian, and G. Popescu, Quantitative phase imaging reveals matrix stiffness-dependent growth and migration of cancer cells, Sci. Rep. **9**, 248 (2019).

[17] S. K. Paidi, P. Raj, R. Bordett, C. Zhang, S. H. Karandikar, R. Pandey, and I. Barman, Raman and quantitative phase imaging allow morpho-molecular recognition of malignancy and stages of B-cell acute lymphoblastic leukemia, Biosens. Bioelectron. **190**, 113403 (2021).

[18] R. Pandey, R. Zhou, R. Bordett, C. Hunter, K. Glunde, I. Barman, T. Valdez, and C. Finck, Integration of diffraction phase microscopy and raman imaging for label-free

morpho-molecular assessment of live cells, J. Biophotonics **12**, e201800291 (2019).

[19] X. Shu, S. Sansare, D. Jin, X. Zeng, K.-Y. Tong, R. Pandey, and R. Zhou, Artificial-intelligence-enabled reagent-free imaging hematology analyzer, Adv. Intell. Syst. **3**, 2000277 (2021).

[20] D. Ryu, J. Kim, D. Lim, H.-S. Min, I. Y. Yoo, D. Cho, and Y. Park, Label-free white blood cell classification using refractive index tomography and deep learning, BME Frontiers **2021**, 9893804 (2021).

[21] Y.-C. Lin, H.-Y. Tu, X.-R. Wu, X.-J. Lai, and C.-J. Cheng, One-shot synthetic aperture digital holographic microscopy with non-coplanar angular-multiplexing and coherence gating, Opt. Express **26**, 12620 (2018).

[22] S. Chowdhury and J. Izatt, Structured illumination diffraction phase microscopy for broadband, subdiffraction resolution, quantitative phase imaging, Opt. Lett. **39**, 1015 (2014).

[23] M. J. Rust, M. Bates, and X. Zhuang, Sub-diffraction-limit imaging by stochastic optical reconstruction microscopy (STORM), Nat. Methods **3**, 793 (2006).

[24] E. Betzig, G. H. Patterson, R. Sougrat, O. W. Lindwasser, S. Olenych, J. S. Bonifacino, M. W. Davidson, J. Lippincott-Schwartz, and H. F. Hess, Imaging intracellular fluorescent proteins at nanometer resolution, Science **313**, 1642 (2006).

[25] S. W. Hell and J. Wichmann, Breaking the diffraction resolution limit by stimulated emission: stimulated-emission-depletion fluorescence microscopy, Opt. Lett. **19**, 780 (1994).

[26] R. W. Boyd, *Nonlinear Optics* (Academic Press, Cambridge, Massachusetts, 2020), Chap. 2.

[27] O. Masihzadeh, P. Schlup, and R. A. Bartels, Label-free second harmonic generation holographic microscopy of biological specimens, Opt. Express **18**, 9840 (2010).

[28] E. Shaffer, C. Moratal, P. Magistretti, P. Marquet, and C. Depeursinge, Label-free second-harmonic phase imaging of biological specimen by digital holographic microscopy, Opt. Lett. **35**, 4102 (2010).

[29] C. Hu, J. J. Field, V. Kelkar, B. Chiang, K. Wernsing, K. C. Toussaint, R. A. Bartels, and G. Popescu, Harmonic optical tomography of nonlinear structures, Nat. Photonics **14**, 564 (2020).

[30] E. Shaffer, P. Marquet, and C. Depeursinge, Real time, nanometric 3D-tracking of nanoparticles made possible by second harmonic generation digital holographic microscopy, Opt. Express **18**, 17392 (2010).

[31] C.-L. Hsieh, Y. Pu, R. Grange, and D. Psaltis, Digital phase conjugation of second harmonic radiation emitted by nanoparticles in turbid media, Opt. Express **18**, 12283 (2010).

[32] E. Shaffer, N. Pavillon, J. Kühn, and C. Depeursinge, Digital holographic microscopy investigation of second harmonic generated at a glass/air interface, Opt. Lett. **34**, 2450 (2009).

[33] D. S. James and P. J. Campagnola, Recent advancements in optical harmonic generation microscopy: applications and perspectives, BME Frontiers **2021**, 3973857 (2021).

[34] M. J. Huttunen, A. Abbas, J. Upham, and R. W. Boyd, Label-free super-resolution with coherent nonlinear structured-illumination microscopy, J. Opt. **19**, 085504 (2017).

[35] E. Wolf, Three-dimensional structure determination of semi-transparent objects from holographic data, Opt. Commun. **1**, 153 (1969).

[36] S. Kang, R. Zhou, M. Brelen, H. K. Mak, P. T. C. So, and Z. Yaqoob, Reflection-mode optical diffraction tomography for label-free imaging of thick biological specimens, arXiv preprint arXiv:2202.13668 (2022).

[37] T. Kim, R. Zhou, M. Mir, S. D. Babacan, P. S. Carney, L. L. Goddard, and G. Popescu, White-light diffraction tomography of unlabelled live cells, Nat. Photonics **8**, 256 (2014).

[38] R. Zhou, T. Kim, L. L. Goddard, and G. Popescu, Inverse scattering solutions using low-coherence light, Opt. Lett. **39**, 4494 (2014).

[39] K. C. Zhou, R. Qian, A.-H. Dhalla, S. Farsiu, and J. A. Izatt, Unified k-space theory of optical coherence tomography, Adv. Opt. Photonics **13**, 462 (2021).

[40] E. G. Steward, *Fourier Optics: an Introduction* (Dover Publications, New York, 2004).

[41] M. G. Gustafsson, Surpassing the lateral resolution limit by a factor of two using structured illumination microscopy, J. Microsc. **198**, 82 (2000).

[42] C. Kuang, Y. Ma, R. Zhou, G. Zheng, Y. Fang, Y. Xu, X. Liu, and P. T. C. So, Virtual k-Space Modulation Optical Microscopy, Phys. Rev. Lett. **117**, 028102 (2016).

[43] T. S. Ralston, D. L. Marks, P. Scott Carney, and S. A. Boppart, Interferometric synthetic aperture microscopy, Nat. Phys. **3**, 129 (2007).

[44] K. Zhanghao, X. Chen, W. Liu, M. Li, Y. Liu, Y. Wang, S. Luo, X. Wang, C. Shan, H. Xie, J. Gao, X. Chen, D. Jin, X. Li, Y. Zhang, Q. Dai, and P. Xi, Super-resolution imaging of fluorescent dipoles via polarized structured illumination microscopy, Nat. Commun. **10**, 4694 (2019).

[45] F. S. Pavone and P. J. Campagnola, *Second Harmonic Generation Imaging* (CRC Press, Boca Raton, Mineola, Florida, 2014).

[46] W.-L. Chen, T.-H. Li, P.-J. Su, C.-K. Chou, P. T. Fwu, S.-J. Lin, D. Kim, P. T. So, and C.-Y. Dong, Second harmonic generation χ tensor microscopy for tissue imaging, Appl. Phys. Lett. **94**, 183902 (2009).

[47] C.-K. Chou, W.-L. Chen, P. T. Fwu, S.-J. Lin, H.-S. Lee, and C.-Y. Dong, Polarization ellipticity compensation in polarization second-harmonic generation microscopy without specimen rotation, J. Biomed. Opt. **13**, 014005 (2008).

[48] I. S. Gradshteyn and I. M. Ryzhik, *Table of Integrals, Series, and Products* (Academic press, Cambridge, Massachusetts, 2014).

[49] M. Gu, *Advanced Optical Imaging Theory* (Springer Science & Business Media, Berlin, 2000), Vol. 75.